3D printing assisted uniformly coated textile for achieving fully flexible supercapacitors with enhanced performance

Journal of Energy Storage 154 (2026) 121017

Contents lists available at ScienceDirect

Journal of Energy Storage

journal homepage: www.elsevier.com/locate/est

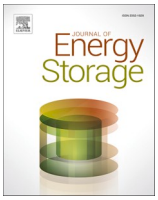

Research papers

3D printing assisted uniformly coated textile for achieving fully flexible supercapacitors with enhanced performance

Soumili Sahoo [a], Viney Ghai [b], Roland Kádár [b,*], Tribeni Roy [a,*]

[a] Department of Mechanical Engineering, Birla Institute of Technology and Science, Pilani, Rajasthan, 333031, India
[b] Department of Industrial and Materials Science, Chalmers University of Technology, Göteborg, 41296, Sweden

ARTICLE INFO

Keywords:
Supercapacitors
3D printing
Energy storage devices
Cyclic voltammetry
Impedance spectroscopy

ABSTRACT

Wearable energy storage devices (ESDs), like batteries, supercapacitors, and hybrids, are currently being explored as possible energy storage solutions for flexible electronics. Textile-based composites show significant potential as electrode materials for ESDs that may lead to the development of smart clothing. However, current methods employed for the deposition of active materials onto textiles show substantial inconsistency, leading to varying electrochemical performance in ESDs, thereby limiting their applicability. Addressing this challenge by achieving uniformity in thin coatings is key to improving the reliability and efficiency of ESDs. This study introduces an innovative method for fabricating fully flexible supercapacitors (SCs) with enhanced performance by utilizing 3D-printed frames to produce wrinkle-free, uniformly coated textile electrodes through a modified hydrothermal dip-coating technique. The approach adopted in this study ensures a uniform coating of the electrode, as revealed by FESEM. XRD study confirms that the layer structure of the electrode materials provides a maximum active surface area for electrochemical performance. Rheological analysis informed that moderate shear rates in the viscosity function reveal an apparent transition to a local shear thickening behaviour. Electrochemical characterization of the fabricated fully flexible SCs reveal impressive metrics, including a specific capacitance (C_s) of 20.39 Fg^{-1}, an energy density (E_d) of 2.54 Wh kg^{-1}, and a power density (P_d) of 160 W kg^{-1}. These SCs demonstrate better stability under mechanical deformation, maintaining 91% Coulombic efficiency even when twisted to 180°. SC can retained C_s up to 95%, 84%, 91.7%, 88%, and 94%, stability after 5000 cycles under various conditions such as no-load, twisting, bending, folding, and washing, respectively. 3D printing-assisted coating method paves the way for creating high-performance, fully flexible SCs.

1. Introduction

The potential uses of wearable electronics in healthcare, defense and fashion industries, among others, have recently garnered attention [1–4]. Most commercially available wearables are not fully flexible due to power source limitations (such as batteries, supercapacitors, etc.). Upon loading, these power sources encounter significant loss in power delivery owing to crack formation/ disintegration/ buckling/ delamination in the electrodes [5]. This limits the advancement of wearable electronics in building fully flexible TVs, smartwatches, smartphones, etc. [6]. Therefore, the key to developing fully flexible wearables lies in building flexible electrodes for batteries/supercapacitors that can retain the capacity of the power source under load. Till date, extensive research has focused on building such flexible electrodes based on substrates that include metal foil [7,8], paper [9], fibre [10], fabric materials [11], etc. Additionally, textile-based supercapacitors (SCs) have been an area of active research owing to their ability to provide excellent electrochemical and mechanical properties. The inherent 3D porous structure of the textile allows electrode mass loading and significantly easier ion movement in the electrodes [12–14]. Electrode fabrication methodology is one of the most crucial steps for ensuring high-capacity retention of SCs under load. Coating the electrode materials onto the surfaces of textiles is very challenging, as the coating process itself can greatly influence the overall electrochemical behaviour of the SCs. The commonly used coating techniques, such as dip coating [15], doctor blade coating [16], screen printing [17], drop casting [18], spray coating [19], etc.

Among these techniques, dip coating is widely used since it offers a simple and scalable approach for depositing active materials (such as carbonaceous materials, metal oxide, and conductive polymer) to synthesize conductive ink onto the textile [20]. The amount of deposited

* Corresponding authors.
E-mail addresses: roland.kadar@chalmers.se (R. Kádár), tribeni.roy@pilani.bits-pilani.ac.in (T. Roy).

https://doi.org/10.1016/j.est.2026.121017
Received 11 October 2025; Received in revised form 23 January 2026; Accepted 6 February 2026
Available online 23 February 2026

conductive ink is determined by the surface properties of the textile, such as its porosity, surface area, conductivity, chemical functionalization, hydrophilicity/hydrophobicity [21,22], adhesion [23], etc. Several studies have explored the potential of dip-coated textiles for SCs electrodes. Hu et al. [24] demonstrated that single-walled carbon nanotube (SWCNTs) onto fabric by dip coating and reported a low electrical sheet resistance of ($<1\ \Omega\ sq.^{-1}$). The resulting electrode exhibited a specific areal capacitance of 35 mF cm^{-2} at a current density of 0.01 mA cm^{-2} with a mass loading of 0.47 mg cm^{-2}. Pasta et al. [25] employed a similar approach for SWCNT-based electrodes, reporting a specific capacitance of 70 F g^{-1} at 0.1 mA cm^{-2}. Yu et al. successfully deposited ~5 nm-thick exfoliated graphene onto polyester fabric using a "*dip and dry*" method, demonstrating its effectiveness for SCs applications [26]. Further studies have highlighted the importance of multiple dip-coating cycles for optimizing electrochemical performance. Fu et al. [27] used different fabric-based electrodes, including Ni wires, carbon fibers, and Au-coated plastic fibers, finding that multiple dip-coating layers were necessary to achieve high capacitance. Jian et al. [28] synthesized Ni_3S_2 on Ni wire electrodes and employed carbon-ink-dipped Ni wire as the counter electrode, achieving a specific capacitance of 34.9 F g^{-1}, an energy density of 8.2 Wh kg^{-1}, power density of 0.81 mWh kg^{-1}, and 93.1% capacitance retention after 3000 cycles. Zhou et al. fabricated electrodes for SCs by dipping cotton fibre thoroughly (five times) in a reduced graphene-oxide solution that showcased a specific capacitance of 5.53 F cm^{-2} [29]. Ye et al. addressed challenges in dip-coating cotton yarns with rGO by uncoiling individual fibers before dipping, resulting in a flexible SCs with a capacitance of 1.85 mF cm^{-3} and excellent rate performance [30]. Barakzehi et al. also deposited rGO on PET/MOF surface by six times 'dip and dry' cycles [31]. Moradi et al. added Fe_3O_4 with graphite to improve the specific capacitance, followed by a similar methodology to deposit active materials on copper foil. Fe_3O_4/graphite showed a Coulombic efficiency with 99% retention after 40 cycles [32]. Deng et al., reported that dip-coating Ni foam twice with a reduced Holy graphene oxide (rHGO)/NiO electrode solution significantly improved capacitance [33]. Lee et al. explored the composition of rGO/multi-walled carbon nanotube (MWCNT) in addition to PEDOT: PSS as an electrode material to study the effect of multiple dip-coating cycles. Initially, the specific capacitance was increased as the number of cycles of dip-coating increased. The optimal number of cycles for dip coating was determined to be five, as this caused excessive mass loading, making it difficult for the flexible fabric to recover its original shape [34].

Despite the promising performance of dip-coated textile electrodes, significant variability remains in the deposition of active materials, as schematically illustrated in Fig. 1. This inconsistency leads to fluctuations in electrochemical performance, making it challenging to achieve uniform, high-performance coatings. To respond to this issue, we have developed a 3D printing-assisted frame (Supplementary Video 1). This frame facilitates the deposition of a uniform coating of the electrode, enabling precise material deposition via a single dip method. The effectiveness of this approach is validated through structural and electrochemical characterization of the coated textiles and their performance under mechanical deformation. Fig. 2 illustrates the overview of the work.

2. Materials & methodology

2.1. Materials

The active materials for electrode preparation included graphite fine (60 mesh) (Loba Chemie Pvt. Ltd., India), acetylene black (Thermo Scientific, USA), Polyvinyl alcohol (PVA, India), and sulfuric acid (H_2SO_4, Sigma Aldrich, US). The textile substrate, polyethene terephthalate (PET, India) textile, was sourced from recycled textiles.

2.2. Preparation of electrode materials

The conductive ink was prepared by dispersing graphite, acetylene black, and polyvinylpyrrolidone (PVP) in an 8:1:1 ratio in deionised water (DIW), followed by continuous stirring using a magnetic stirrer for 24 h at 1500 rpm. Simultaneously, various textile samples were collected from waste and cut into the desired shapes, which is a cost-effective solution [35]. These textiles were thoroughly rinsed with DIW to eliminate stains, impurities, and residual contaminants, followed by oven drying for 1 h to ensure complete moisture removal.

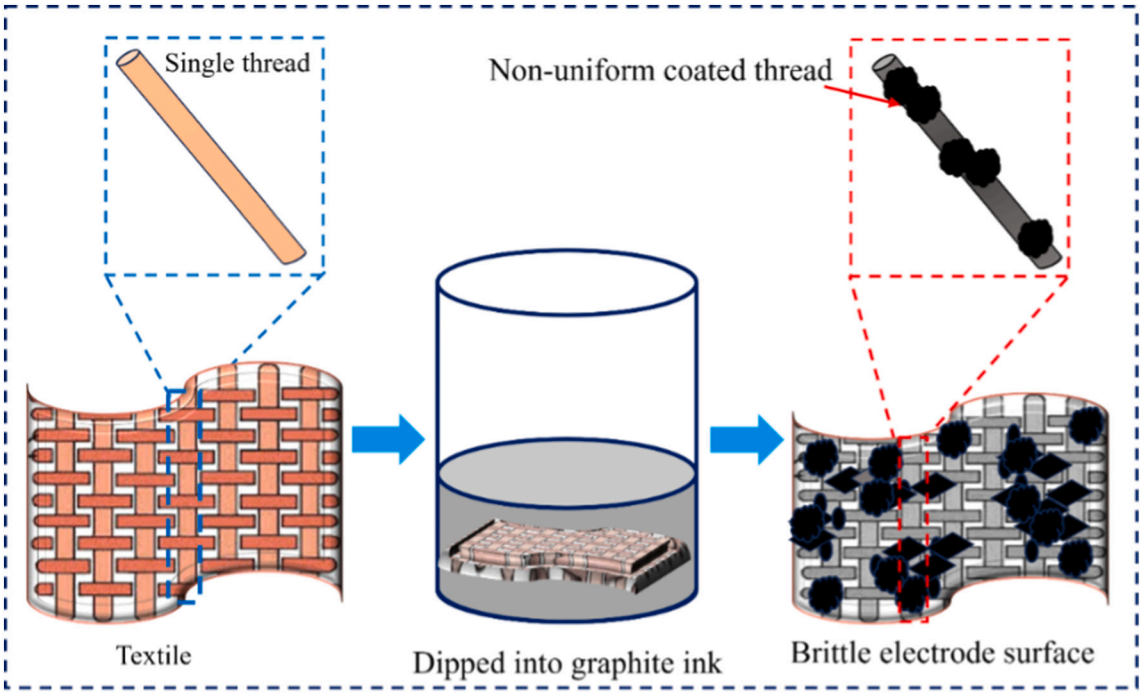

Fig. 1. Schematic of conventional dip coating methodology, illustrating the process flow and emphasizing the limitation of inconsistent coating distribution across the textile.

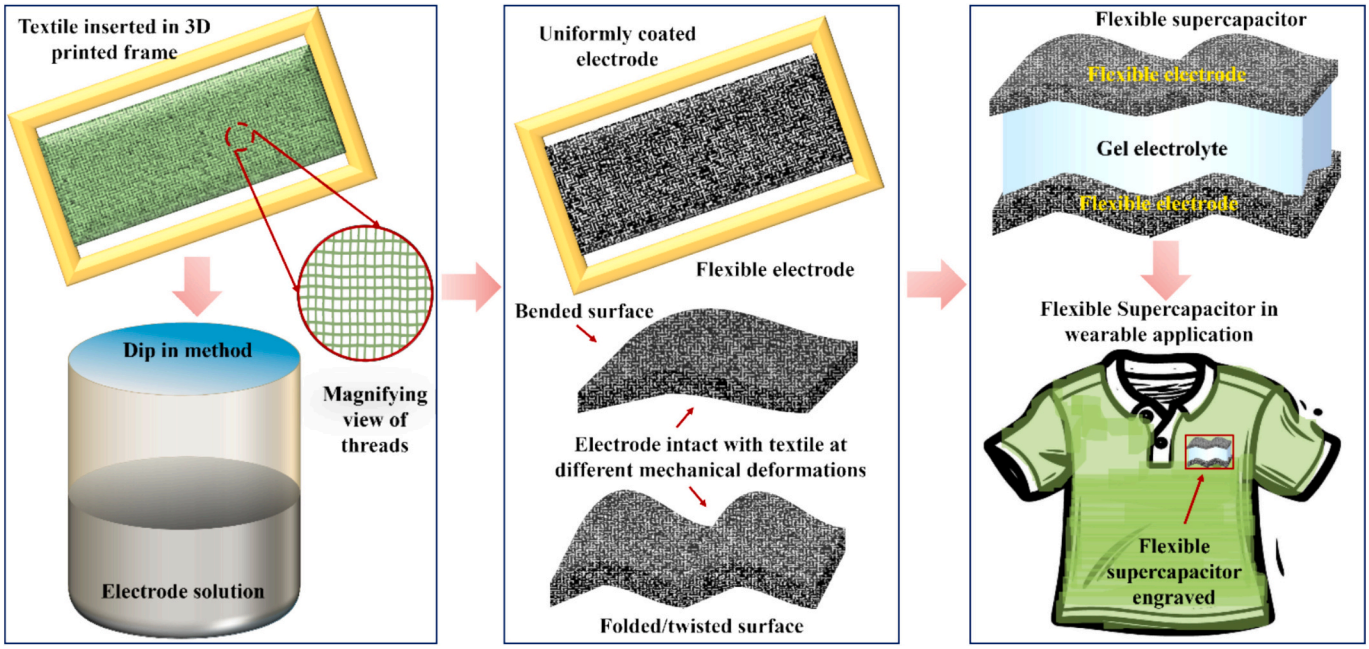

Fig. 2. Provide an overview of the work, along with its potential applications.

2.2.1. Flexible electrode fabrication

The key to achieving uniformity in coating active materials on textiles lies in ensuring that the textile is uniformly wetted and dried by the active materials, making it wrinkle-free and fully flexible. To achieve this, a customized 3D-printed frame with a sliding mechanism was developed. The 3D-printed frame is the primary innovation of this work, generating consistent mechanical tension in the textile. The frame is fabricated using a lightweight PLA (polylactic acid) filament with a layer resolution of 0.2 mm. It consists of two opposing rails and a sliding carriage mechanism. This mechanism is designed to maintain the wrinkle-free surface of the textile during electrode deposition. The textile is held in the movable clamp. Then the movable clamps slide

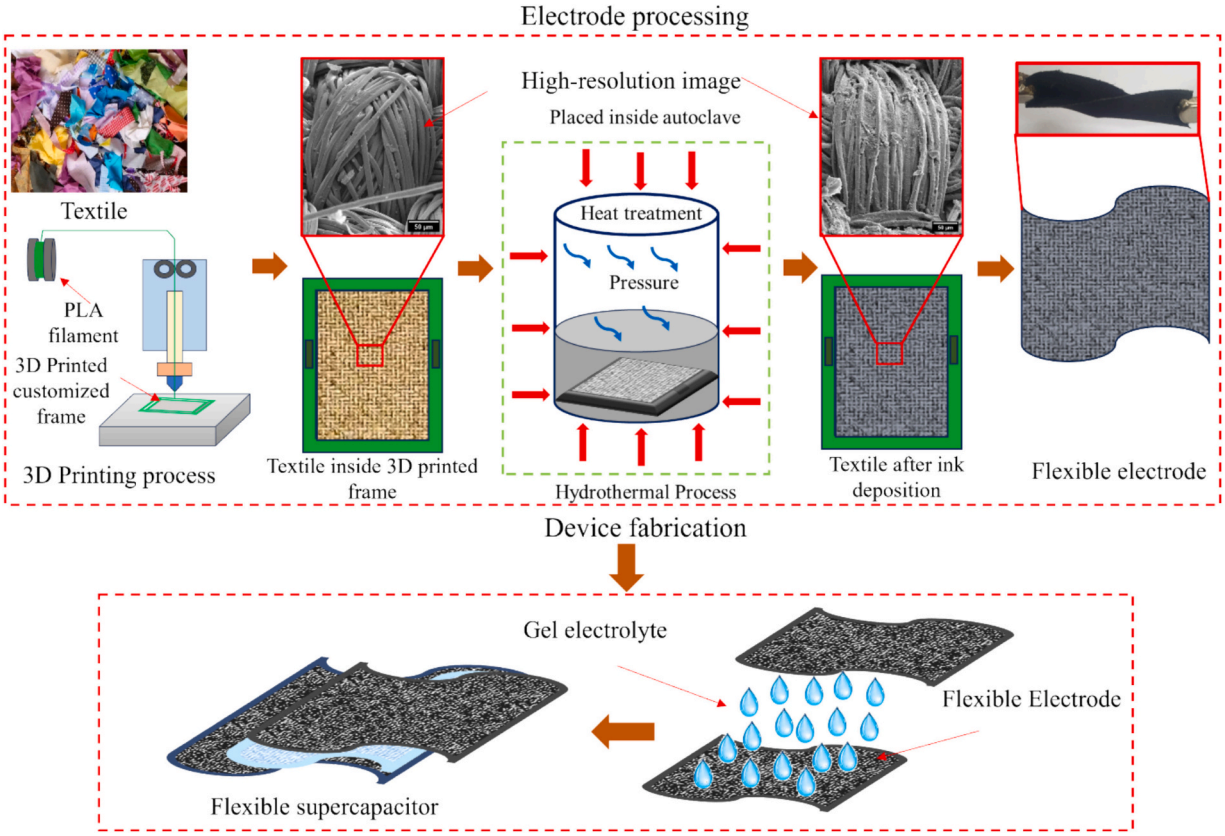

Fig. 3. Detailed schematic illustrating the fabrication stages of a textile-based flexible supercapacitor, highlighting the integration of 3D printed frame, autoclave treatment, flexible electrode preparation, gel electrolyte synthesis, and final device assembly.

along a predefined path inside the fixed clamp (Fig. S2). Then the textile is stretched fully and locked in place. This frame provided a stable platform for mounting the textile before depositing the conductive ink, preserving its structural integrity throughout the experiment. This controlled tension prevents wrinkle formation and ensures a smooth, straight surface, as shown in Supplementary Video 1. Additionally, it facilitated precise alignment and maintained the necessary tension, keeping the textile straight, taut, and evenly supported. This stability was essential for ensuring uniformity across the textile surface and played an important role in achieving a uniformly coated surface. Supplementary Video 1 demonstrates the working of the frame. The sliding clamp mechanism provides precise and repeatable tension control on the surface. This mechanism distinguished our approach from the conventional method.

To achieve a uniform, smooth, and wrinkle-free surface without brittle regions, a modified dip-coating process was employed, as shown in Fig. 3. The hydrothermal process was used to enhance the adhesive bond between the electrode and the textile. The textile was mounted on the frame and dipped in conductive ink. Then the dipped textile was placed in an autoclave and heated in a hot-air oven at 80 °C for 12 h to facilitate drying. After cooling, the textile was carefully removed from the frame and subjected to a secondary drying step at 50 °C for 2–3 h under ambient conditions.

2.2.2. Electrolyte preparation & fabrication of SCs

A gel electrolyte was used in this work for the fabrication of SCs. The PVA/H_2SO_4 gel serves as an electrolyte and a separator, thereby remarkably reducing the overall cost and weight of SCs. Moreover, the gel electrolyte effectively prevents leakage, thereby enhancing the safety and flexibility of the SCs.

For the preparation of gel electrolyte, 3 g of PVA was dissolved in 30 mL of DIW and heated at 85 °C until fully dissolved. Subsequently, 3 g H_2SO_4 was gradually added to the solution. The resultant gel electrolyte was then sandwiched between two symmetric flexible electrodes to fabricate fully flexible SCs (Fig. 3).

2.3. Characterization techniques

Surface morphology of the coated textile was characterized using FEI Quanta FEG 250 field emission scanning electron microscopy (FESEM). X-ray diffraction (XRD) was carried out using Bruker D2 Phaser to analyze the crystal structure and phase. To understand the chemical composition and structural defects of electrode material, Raman Spectroscopy (HORIBA, AIST-NT, Labram HR Evolution, Omega Scope) was analyzed. To gain insight into the properties of the electrode and electrolyte, we conducted rheological characterization using an Anton Paar (Graz, Austria) rotational rheometer with a profiled bob and cup measuring geometry (CC27/P6). The cup has an inner diameter of 29 mm, while the bob has an outer diameter of 27 mm. The measurements were carried out in a single motor-transducer configuration at 23 °C. For the evaluation of the electrochemical behaviour of the SCs, an AUTOLAB PGSTAT203N (Metrohm) was used for cyclic voltammetry (CV), galvanostatic charging & discharging (GCD), and electrochemical impedance spectroscopy (EIS).

These measurements were performed at an open-circuit potential across the frequency range of 0.01 Hz to 100 kHz at a 5 mV open-circuit potential (OCP). The specific capacitance (C_s), CV, and GCD results were calculated based on Eqs. (1)–(2) as follows [10,36]:

$$C_s = \frac{\int_{V_1}^{V_2} i(V)\, dv}{2{*}m\gamma\Delta V} \tag{1}$$

$$C_s = \frac{I\Delta t}{m\Delta V} \tag{2}$$

For CV, the C_s is derived from the area under the curve by integrating $\int_{v_1}^{v_2} i(v)\, dv$ where V_1 and V_2 represent the lower and higher window voltage limits. Here, m signifies the mass of the active electrode materials, γ indicates the applied scan rate, and ΔV is the potential window. For GCD curves, I is the discharge current (A), and Δt is the discharging time in seconds. The energy density (E_d) and power density (P_d) are computed using Eqs. (3)–(4) respectively.

$$\text{Energy density}, E_d = \frac{C_{sp}\nabla v^2}{7.2} \tag{3}$$

$$\text{Power density}, P_d = \frac{E_d{*}3600}{\Delta t} \tag{4}$$

3. Results & discussion

The rheological properties of the electrolyte and electrode materials provide insight into the material design requirements for achieving optimal textile integration and enhanced electrical performance and reproducibility. The viscosity functions depicted in Fig. 4(a) show markedly different material behaviour. The electrolyte (Fig. 4(b)) exhibits a standard zero-shear viscosity plateau followed by progressive shear thinning. We note, however, that within the shear rate range investigated, a range that includes shear rates relevant to dip-coating operations, the steady shear viscosity of the electrolyte varies by only 20–40%, making the coating thickness uniformity less sensitive to the withdrawal speed [37]. The strain amplitude sweep data in Fig. 4(d) shows a viscous-dominated viscoelastic material response, $G'' \gg G'$, but with a measurable storage modulus G'. In contrast, the electrode material (Fig. 4(c)) potentially shows a more complex material rheological response. The viscosity function at low shear rates in Fig. 4(a, b) together with the gel-like linear viscoelastic response in Fig. 4(d) confirms the presence of a yield stress. Interestingly, moderate shear rates in the viscosity function reveal an apparent transition to a local shear thickening behaviour. While we have observed drying of the free surface of the sample during testing, we note that a strain-stiffening behaviour could be observed at shear strain amplitudes that correspond to shear rate amplitudes very similar to the thickening range observed in steady shear. By considering the crossing between the dynamic moduli in nonlinear viscoelastic region of the strain amplitude test as an approximate measure of a breaking point of the network responsible for the gel-like behaviour, it could be inferred that this corresponds to the transition between the shear thinning and shear thickening regions of the viscosity function. We note that the approximate measure of this critical strain amplitude is due to the fact that linear viscoelastic moduli are determined under the hypothesis of a sinusoidal material response, which is not valid in the nonlinear region.

Fig. 5 compares the textile electrodes obtained via conventional dip coating with those obtained using a modified approach with a 3D printing-assisted setup. In the case of conventional dip coating, noticeable agglomerations of active material are evident on the textile surface even before mechanical deformation, indicating non-uniform deposition. In contrast, the 3D printing-assisted method yields a smooth, homogeneously coated textile with no visible agglomeration. To evaluate mechanical robustness, a qualitative twisting deformation was applied to both samples. The conventionally coated textile showed significant material detachment during twisting (highlighted by the red circle), demonstrating poor adhesion and mechanical integrity. Conversely, the textile coated using the 3D printing-assisted method remained intact and wrinkle-free, maintaining uniformity under mechanical stress. This improvement can be attributed to the 3D-printed customized frame, which provided structural support and maintained constant tension, ensuring the textile remained flat, aligned, and evenly supported throughout the coating process. Additionally, a hydrothermal treatment was employed at pressure and temperature to further enhance the adhesion between the conductive ink and the textile substrate. The following sections provide a detailed analysis of the surface morphology

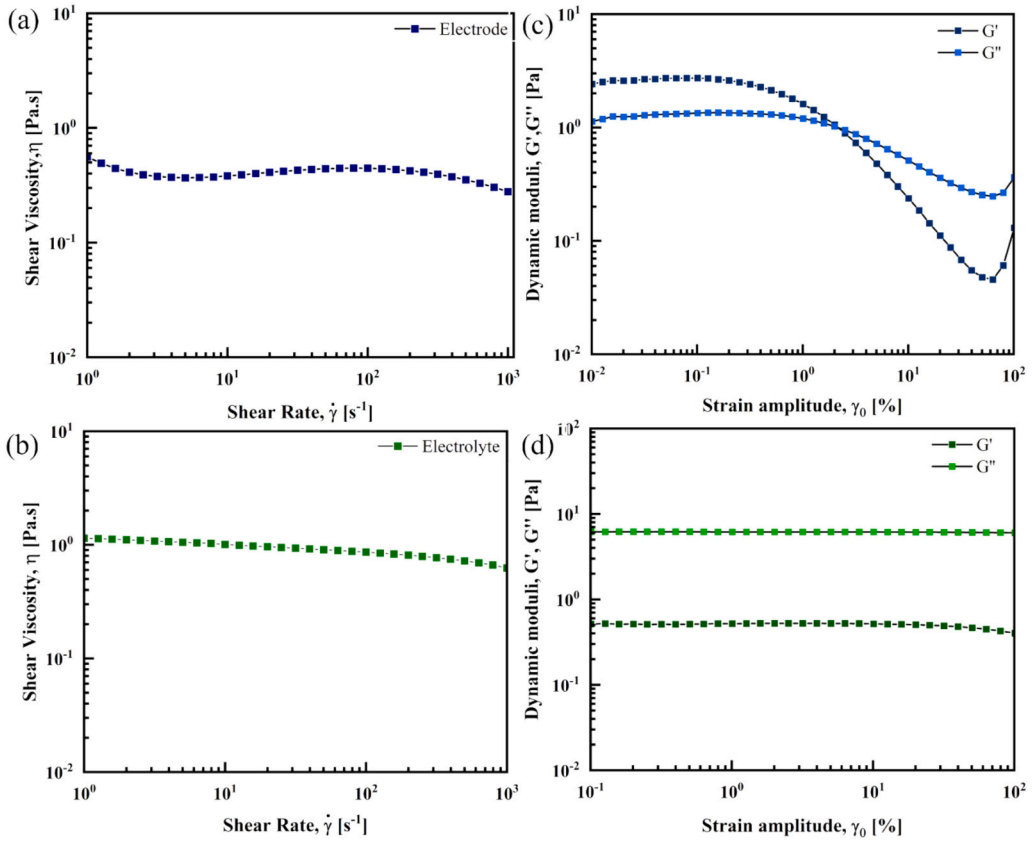

Fig. 4. Flow curve of the electrode and electrolyte. (a) Viscosity of the graphite electrode and gel electrolyte solution as a function of shear rate. (b) Storage modulus (G′) and loss modulus (G″) as a function of Strain amplitude (γ_0) for both materials at 6 rad/s.

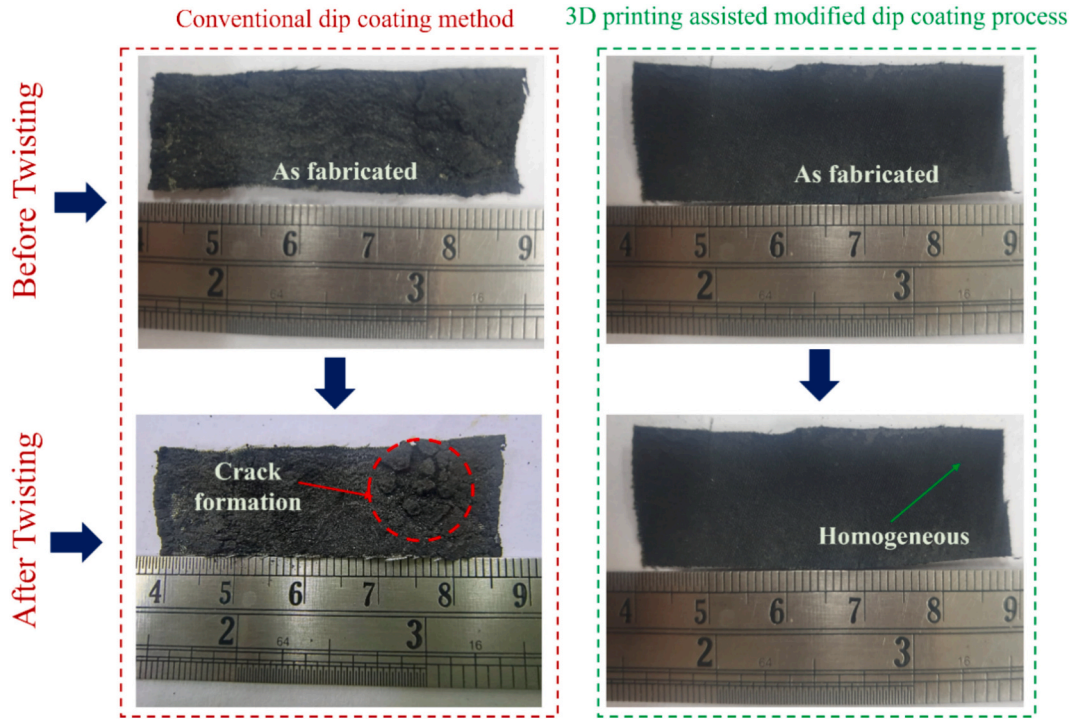

Fig. 5. Demonstration of the differences between conventional dip coating and 3D printing-assisted modified dip coating, highlighting the twisting effect before and after.

and electrochemical performance of the resulting electrodes. Supplementary Video 2 demonstrates the electrode deposited through

conventional dip coating, while Supplementary Video 3 represents the electrode deposited using our approach.

3.1. Flexible electrode characterization

3.1.1. Surface morphology of flexible electrode via imaging

Figs. 6–7 presents the top-view and edge-view surface morphology of the fabricated flexible electrode. As shown in Fig. 6, high-resolution imaging reveals a uniform and continuous coating of graphite ink across the textile surface. The initial thread thickness of the pristine textile specimen analyzed was approximately 10.71 μm, which increased by around 2.37 μm after the coating process, indicating a consistent deposition of the active material. The graphite ink appears evenly distributed across the entire textile, with a well-defined graphitic layer enveloping the individual fibers. Further magnification reveals a distinct layered structure, suggesting strong adhesion between the deposited graphite and the textile substrate. Such a morphology is advantageous, as previously reported studies have shown that a layered architecture not only enhances the available active surface area for electrolyte ion absorption [38]. These behaviours are essential for electric double layer capacitance as ions can penetrate between the sheets and generate a compact Helmholtz layer at the electrode-electrolyte surface. The Helmholtz layer facilitates ion transport and also enables charge accumulation during the electrochemical process. The layered structure of the control samples correlates with a lower current response in the electrochemical behaviour [39]. This nature confirms that surface texture and ion accessibility strongly influence capacitive performance. The combination of the 3D printing-assisted dip coating method and subsequent hydrothermal treatment is likely responsible for the enhanced coating uniformity and improved adhesion. As a result, the overall electrode structure and electrochemical integrity were improved.

To obtain a more detailed insight into the coating quality, an edge-view analysis was carried out for the uncoated textile (Fig. 7(a)), coated textile (Fig. 7(b)), and coated textile after electrolyte deposition (Fig. 7(c)).

Fig. 7(a) exhibited the thickness of the pristine textile of ~60 μm. Upon application of the graphite ink, an evenly coated textile was observed similarly to Fig. 6. The porous architecture of the textile facilitated enhanced absorption of the conductive ink during the hydrothermal process, enabling a more uniform and dense coating over a larger surface area than that achieved by conventional dip-coating methods, as illustrated in Fig. 7(b). The deposition of the gel electrolyte, as shown in Fig. 7(c), effectively penetrates through the electrode. This is accelerated by the layered structure of the electrode material, which forms an extensive network of pathways [40]. These pathways enable the electrolyte to access a maximum surface area of the electrode, thereby enhancing the interaction between the electrode and the electrolyte interface. As the electrolyte permeates the structure, it interacts with a greater number of electrochemically active sites, promoting more efficient ion transport and redox reactions. This increased interfacial area and improved ion accessibility significantly boost the charge storage capacity, thereby enhancing the overall performance of the SC. This is further explained in Section 3.2.

3.1.2. Crystal structure and chemical defects of flexible electrode

Raman spectroscopy was employed to analyze the structural characteristics of the graphite-coated textile, which is presented in Fig. 8(a). The Raman spectrum displays prominent peaks corresponding to the first-order D band (~1336 cm^{-1}), first-order G band (~1581 cm^{-1}), and the second-order 2D band (~2688 cm^{-1}). Additionally, weaker peaks observed at ~1096 cm^{-1} and ~1728 cm^{-1} are attributed to the underlying textile substrate. Compared to previously reported values [41], the slight redshift of the D band suggests strong interfacial interaction between the graphite and the textile substrate. The intensity of the G band was higher than the intensity of the D band, where the I_D/I_G ratio was 0.39. This value suggests a higher degree of graphitization and the formation of fewer structural defects in the deposited graphite [42]. This ratio also implies good uniformity and consistent layer distribution of the graphite ink on the textile surface [43].

The XRD analysis was performed to investigate the structural characteristics and phase composition of the flexible electrode, as depicted in Fig. 8(b). Prominent diffraction peaks observed at 2θ values of 27.2°, 42.6°, and 46° correspond to the (002), (100), and (101) crystal planes of graphite, respectively, in accordance with JCPDS Card No. 75-1621. The interplanar spacing (d spacing) for the (002) plane at 27.2° was calculated using Bragg's law, yielding a value of approximately 0.377 nm [44]. This is in agreement with previously reported values for graphitic materials [45], indicating that the hydrothermal process did not disrupt the crystallinity of the graphite structure. Furthermore, the hydrothermal treatment is believed to have enhanced the uniformity of the coating by promoting controlled nucleation and deposition of the graphite, thereby preventing the formation of agglomerates or uneven layers. This uniform and thin coating also contributed to improved mechanical integrity of the flexible electrode, as evidenced by its strong adhesion to the textile substrate (Fig. 5). In addition, diffraction peaks exhibited at 2θ of 17.1°, 22.6° and 26.2° were observed, corresponding to the (010), (110), and (100) planes of the textile material, confirming the preservation of the fabric structure beneath the conductive layer.

3.2. Electrochemical analysis

To comprehensively asses the electrochemical behaviour of the fabricated SCs using flexible electrodes synthesized by our approach, a series of electrochemical characterization were employed. These included cyclic voltammetry (CV), galvanostatic charging discharging (GCD), and electrochemical impedance spectroscopy (EIS). Additionally, the effect of mechanical deformation, specifically twisting the SCs at various angles, on their electrochemical behaviour was investigated. For CV analysis, measurements were conducted at scan rates of 5, 10, 50, and 100 mV s^{-1} within a potential range of −0.4 to 0.4 V. GCD tests were performed at current densities of 0.018 and 0.02 A g^{-1} within a voltage

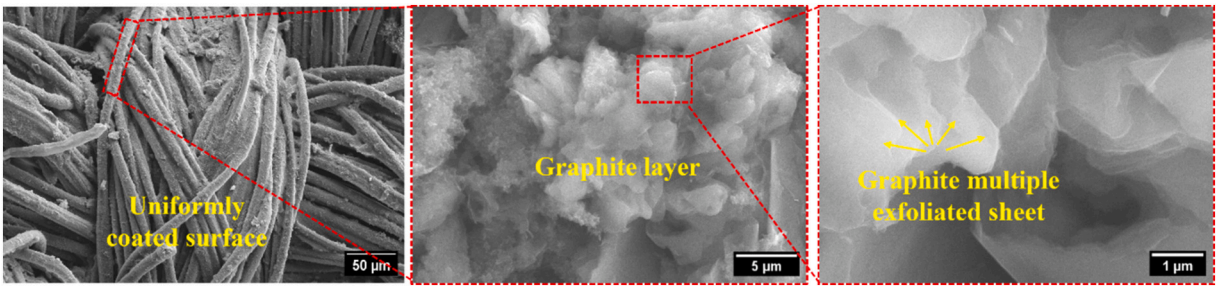

Fig. 6. FESEM analysis of graphite-coated textile electrode: Surface morphology showing homogeneous graphite layer on the textile substrate; magnified image of graphite ink distribution, revealing features; multilayer graphite sheet formation through textile cross-section, demonstrating exfoliated deposition of graphite sheet.

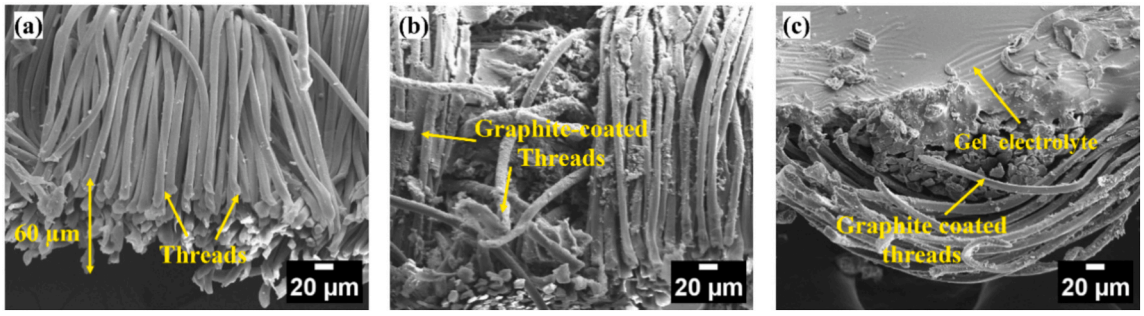

Fig. 7. Edge-view FESEM micrographs illustrating the textile electrode: (a) Pristine textile (b) Textile threads with uniform graphite ink coating, and (c) Gel electrolyte integration, showcasing penetration through the electrode material.

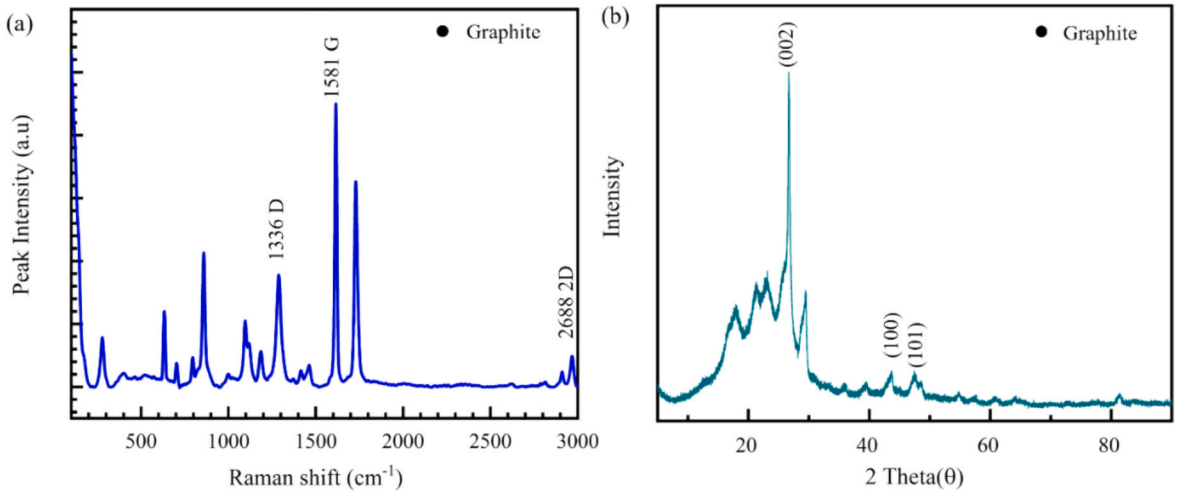

Fig. 8. Spectroscopic analysis of graphite ink electrode: (a) Raman spectrum illustrating graphitic features, and (b) XRD pattern revealing lattice structure and crystallinity.

window of 0.8 V to assess charge-discharge behaviour. The negative potential window was selected because graphite exhibits the most stable and reversible electric double-layer behaviour under cathodic polarization [46,47]. EIS analyses were conducted over a frequency spectrum ranging from 0.01 Hz to 100 kHz, with an applied amplitude of 5 mV, under open circuit potential (OCP) conditions.

The electrochemical performance of a fabricated electrode was compared with the presented method against the conventional dip coating process. The SC using both electrodes was electrochemically characterized, including CV, GCD, and EIS. This analysis is represented in Fig. S1. Fig. S1(a) reveals that the electrode synthesized through this approach exhibits 17.6% higher C_s. Additionally, GCD analysis (Fig. S1 (b)) shows 17.9% higher Coulombic efficiency. Fig. S1(c) represents the EIS analysis of both cases. The nature of the curve indicates relatively better charge storage and ion transport compared to the conventionally dip-coated electrode. Based on this performance, subsequent investigations focused on SC fabricated using the approach method. Furthermore, the electrochemical characterization of SCs was evaluated under various mechanical deformations, including twisting, bending, folding, and repeated washing, to understand their mechanical robustness for real-world wearable electronics applications. Supplementary Video 4 represents the twisting condition, whereas Supplementary Video 5 represents the bending condition.

3.2.1. *Insights from cyclic voltammetry (CV)*

To evaluate the specific capacitance (C_s) of the developed supercapacitors (SCs) under different mechanical deformations, cyclic voltammetry (CV) measurements were performed on samples subjected to twisting angles of 60°, 120°, and 180°, as well as on untwisted samples. The corresponding CV curves are presented in Fig. 9(a–d), which is nearly rectangular in shape. The near-rectangular shape at low scan rates indicates electric double-layer capacitance arising from rapid adsorption–desorption of electrolyte ions at the carbon-rich surface. The gradual deviation from ideal rectangularity at higher scan rates reflects increased resistance and diffusion limitations in the pore network [48]. The nature of CV curves indicates the capacitive behaviour of the electrode material. It is also noted that the capacitive behaviour is dominated by surface charge accumulated at the electrode-electrolyte surface. There are no such peaks observed in CV curves, which demonstrates that no redox reaction occurs inside the materials [49].

As the twisting angle increased, a gradual reduction in the integrated region within the CV curve was observed. This curve shows the stability with a gradual decrease at 180°, particularly at higher scan rates. This reduction signifies a drop in electrochemical performance due to mechanical strain. Nevertheless, the SCs maintained stable operation over different scan rate, suggesting that the electrode integrity remained largely intact unlike in the case of conventional dip-coated electrodes, where significant material delamination was observed (Fig. 5). Under no load condition, a specific capacitance (C_s) was 20.39 Fg^{-1} at a lower scan rate of 5 mVs^{-1}, while for same scan rate, the 180° twisted sample exhibited a C_s of 12.05 Fg^{-1} (Fig. 9(a)), indicating a 40% reduction in C_s. Despite increasing the scan rate to 100 mV s^{-1}, the SCs deliver a C_s of 2.48 F g^{-1} (Fig. 9(d)), demonstrating the SCs' good storage capability and mechanical stability. These properties of SCs are crucial for application as power sources in flexible and wearable electronics. These results highlight that achieving a C_s value significantly influenced by a

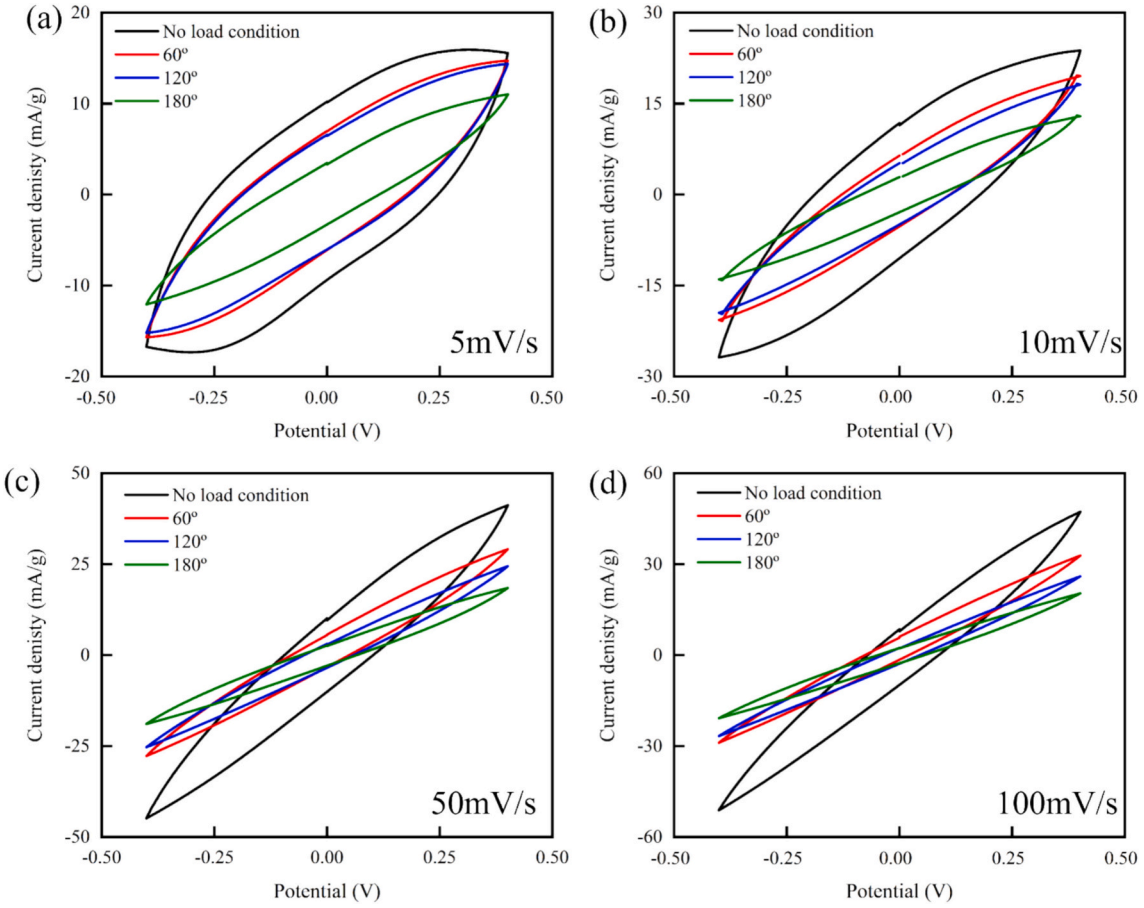

Fig. 9. Comprehensive analysis of flexible energy storage device performance: CV profiles at (a) 100 mV s^{-1}, (b) 50 mV s^{-1}, (c) 10 mV s^{-1}, and (d) 5 mV s^{-1}; Impact of scan rate and mechanical deformation (twisting angle at 60°, 120° and 180°) on specific capacitance.

uniform coating on the electrode, illustrating the importance of uniform mass loading and representing better performance [45].

Compared to the no-load condition, the specific capacitance decreased to 94.7%, 91.2%, and 59.0% at twisting angles of 60°, 120°, and 180°, respectively, at a scan rate of 5 mV s^{-1}, as illustrated in Fig. 10 (a). However, capacity retention decreases to 85% (60°), 52.4% (120°), and 41.13% (180°). These degraded results were obtained by applying continuous twisting with a 30° interval. Such incremental twisting slowly impacts the SC as shown in Fig. 10(b). Further assumed that the absence of continuous changes during direct twisting reduces degradation and highlights the importance of uniform electrode coating for stability. Notably, the impact of continuous twisting has not been explored, with existing research primarily on direct twisting. Fig. S2 presents the CV performed at various scan rates ranging from 5 to 100 mV s^{-1} within the potential window of −0.4 to 0.4 V under different twisted angles of 30°, 60°, 90°, 120°, 150°and 180°.

In addition to twisting, in Fig. 10(c, d, e and f), the SC was evaluated under bending and folding conditions. To understand the SC's realistic application, consider the conditions under which wearable electronics are washed (Fig. 10(g)). The obtained CV curve after each deformation mode observed a capacitive shape, indicating that the electric double-layer charge storage mechanism remains effective. Fig. 10(c) represents the bending tests at angles of 60° and 90°. At 60° bending angle, the C_s decreases from 20.39 F g^{-1} to 19.87 F g^{-1}, while a more noticeable reduction to 15.92 F g^{-1} is observed at 90° bending (Fig. 10(d)). In the case of folding, an 8.44% capacitance loss was observed, as shown in Fig. 10(f), at lower scan rates (5 mV s^{-1}). This capacitance loss due to simple localised strain was applied at the electrode-electrolyte interfaces. This localised strain restricted ion transport in the PVA/H_2SO_4 gel electrolyte (Fig. 10(f)).

To understand durability after washing, SC was immersed in a common detergent solution for 5 min (1 min/cycle, repeated five times) (Fig. 10(g)). The detergent-washed SC retains 82% of its initial capacitance, likely due to weakened interfacial bonds with the electrolyte or a small degree of electrode material degradation (Fig. 10(h)). Future analysis of the degradation of the electrode, it was dipped into the normal water and detergent water for 24 h as shown in Fig. S4. Fig. 11(a) represents the initial structure of SC and electrolyte bonding between polymer PVA and H_2SO_4. These results confirm that, among all mechanical deformations, twisting shows the most significant decline in performance. This declined behaviour can be attributed to the nature of torsional strain, which induces simultaneous shear and tensile stresses across the electrode and electrolyte, shown in Fig. 11(b). The combination of multiple strains is more effective, and it disrupts the continuous pathway within SC. As the twisting angle increases, the pathway becomes narrower, as shown in Fig. 11(b); consequently, internal resistance increases. In contrast, bending at 60° and 90° introduces uniaxial strain. This strain can be partially accommodated by the inherent flexibility of the graphite layer and the polymer gel electrolyte, resulting in better capacitance retention (Fig. 11(c)) [50]. Fig. 11(d) clearly shows that the folding generates multiple local strain that affects a limited region of the SC. Therefore, a smaller overall impact occurs on the effective charge-storage area [51]. These results highlight smaller changes observed after applying bending and folding to the SC electrode–electrolyte.

3.2.2. *Galvanostatic charging discharging (GCD) behaviour of SCs*

Fig. 12 demonstrates the GCD profile of fabricated SCs with various

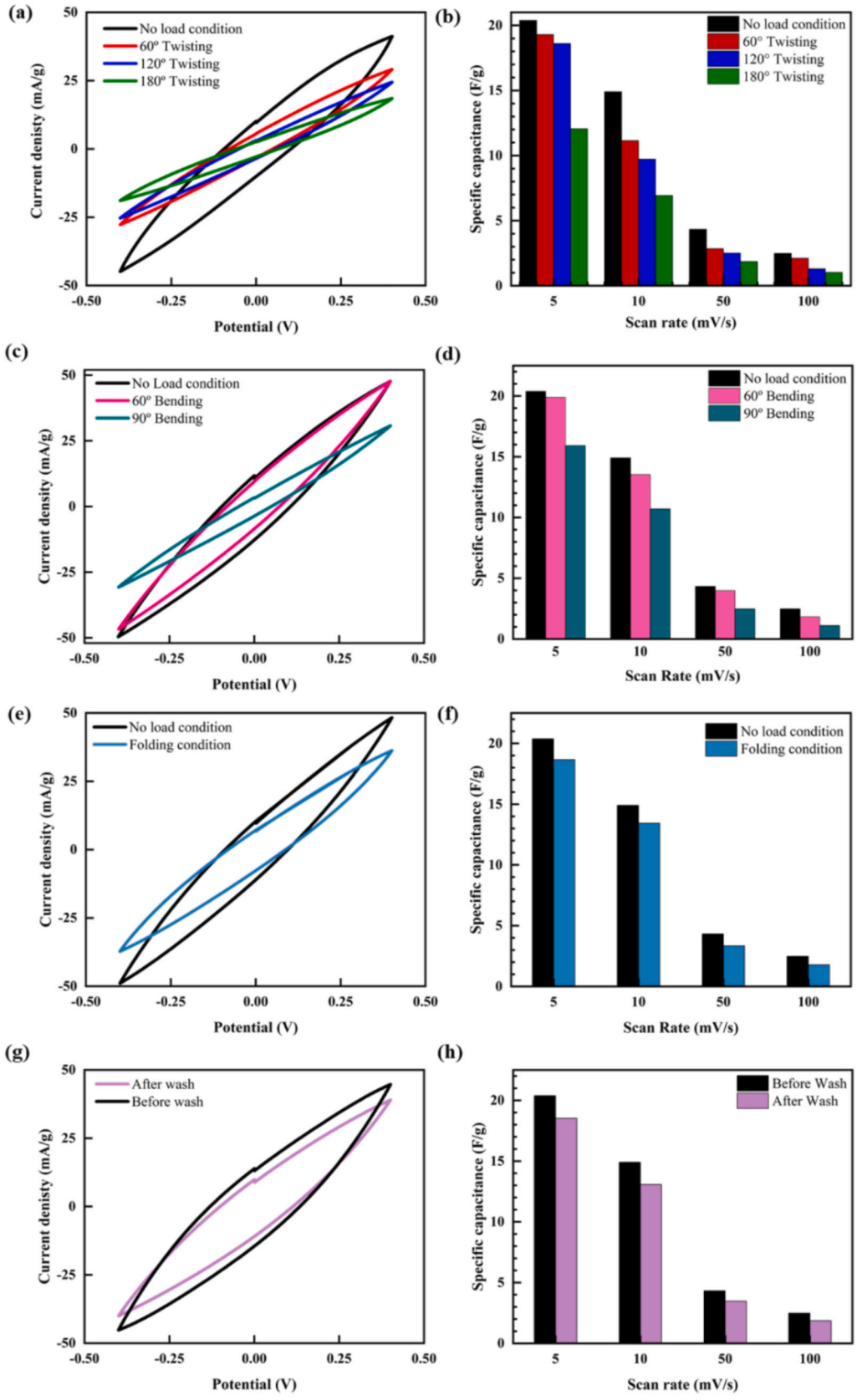

Fig. 10. Electrochemical of the flexible SC under different mechanical deformation conditions. (a, c, e and g) represent the CV recorded under twisting, bending, folding, and washing conditions, respectively, demonstrating the retention of capacitive behaviour under mechanical stress. (b, d, f and h) illustrate specific capacitance as a function of scan rate corresponding to the same deformation modes, highlighting the progressive reduction in accessible capacitance with increasing mechanical severity, particularly under extreme twisting and folding.

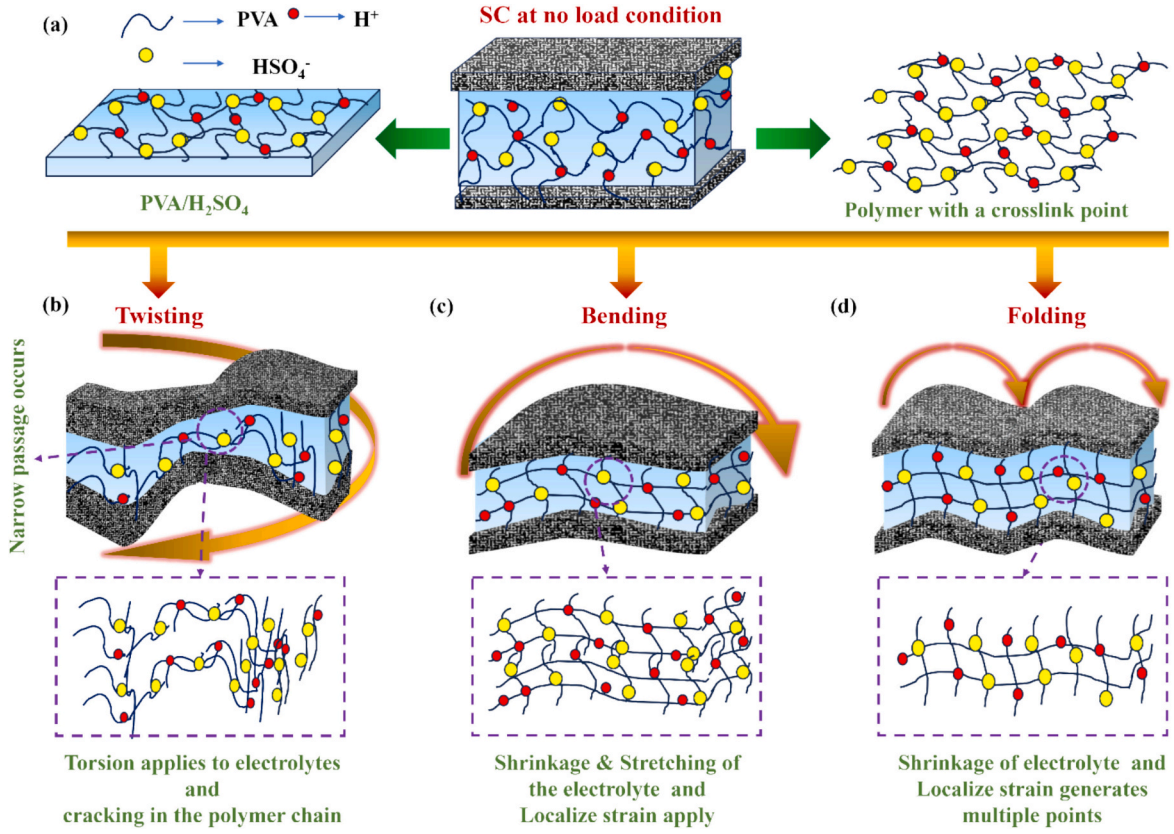

Fig. 11. Representative of deformation-induced changes within the electrolyte under twisting, bending and folding. (a) Structural representation at no load condition, (b) represents a narrow passage that occurs, making it difficult for ion movement, (c) bedding shows localised strain applied and (d) shrinkage of electrolyte.

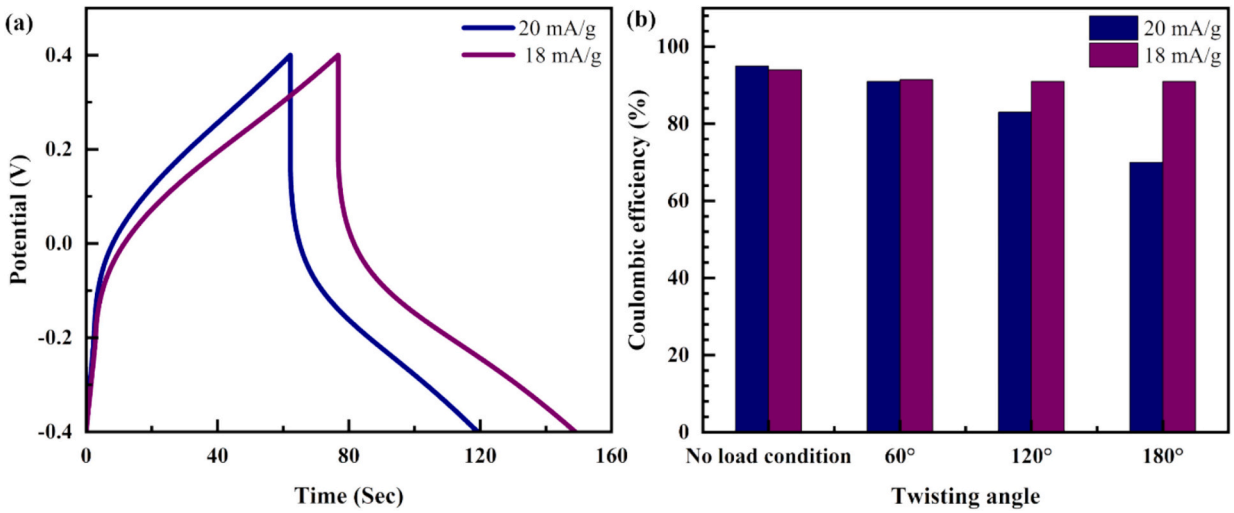

Fig. 12. The GCD behaviour of the flexible SCs: (a) at 20 mA g^{-1} & 18 mA g^{-1}, (b) Coulombic efficiency at the same current density, demonstrating the effect of different twisting angles and different current densities.

twisting angles. GCD analysis was performed at a current density of 20 mA g^{-1} and 18 mA g^{-1}, as shown in Fig. 12(a). Qualitatively, the GCD curves exhibit a similar triangular shape, suggesting a good capacitive response. Minor deviations in the charge-discharge profile were observed across the different twisting angles, demonstrating the SC's mechanical flexibility and stable electrochemical performance under deformation.

The charge-discharge duration at a current density of 20 mA g^{-1} is shorter than that of 18 mA g^{-1}, consistent with the faster kinetics at higher current densities. The SC exhibits C_s 28.51 F g^{-1} at a current density of 20 mA g^{-1} and shows 21.07% higher C_s at a current density of 18 mA g^{-1}. Similarly, as shown in Fig. 12(b), the fabricated SC exhibited Coulombic efficiencies of 94%, 91.5%, 91%, and 91% at a current density of 18 mA g^{-1}. At a current density of 20 mA g^{-1}, the fabricated SC exhibited Coulombic efficiencies of 95%, 91%, 83%, and 70% under no-load, 60°, 120°, and 180° twisting conditions, respectively. Incremental twisting from no load to 180°, with measurements taken at each interval, resulted in a Coulombic efficiency of approximately 70%. The

high Coulombic efficiency may be attributed to the improved coating from previously reported literature, which was achieved by the 3D printing-assisted modified dip coating method [52,53].

The charge–discharge behaviour of the flexible SC was investigated under twisting, bending, folding, and washing conditions to evaluate the impact of mechanical deformation, observed in Fig. 13. After mechanical deformation, the charging-discharging triangular profile is maintained for all deformation modes, confirming that the device remains electrochemically operational. However, the discharge time decreases with increasing mechanical harshness, reflecting a reduction in effective capacitance [48].

The GCD curve shows C_{sp} 28.51 Fg^{-1}, 13.55 Fg^{-1}, 9.87 Fg^{-1} and 5.19 Fg^{-1} at no load condition, 60°, 120° and 180° twisting angle at 20 mAg^{-1} as observed in Fig. 13(a). This reduction indicates a rise in internal resistance due to the torsional strain-induced disruption of conductive pathways within the electrode and a partial loss of interfacial contact with the PVA/H_2SO_4 gel electrolyte (Fig. 11(b)). In contrast, bending at 60° and 90° shows relatively minor reductions in discharge time, with capacitance retention of 88.5% and 75%, respectively (Fig. 13(b)). This suggests that uniaxial bending strain as shown in Fig. 11(c) can be more effectively accommodated by the flexible electrode–electrolyte architecture. Folding and washing exhibit 82.2% and 81% capacitance retention compared to the no-load condition Fig. 13(c) &(d). Folding affects a strain in the confined region of the SC, limiting the overall impact on the effective charge-storage area (Fig. 11(d)). While washing induces only moderate changes in discharging behaviour due to degradation of electrolyte bonding, as exposed to detergent water. The quasi-linear charge–discharge slopes under these conditions indicate that ion transport within the gel electrolyte and charge adsorption at the graphite surface remain largely reversible [54]. Overall, the GCD analysis validates the CV results, demonstrating that torsional deformation is the most disadvantageous mode for the SC. Whereas bending, folding, and washing impose comparatively smaller drawbacks on charge–discharge performance.

This charging-discharging behaviour was observed due to the formation electric double layer. The electric double layer consists of the inner (Helmholtz) layer and outer (diffuse) layer. The compact Helmholtz layer creates a very small non-Faradaic charge separation, due to electrostatic interactions. The presence of a diffusion layer in electrode materials helps in the dispersion of ions near the surface [55]. The extent of this double-layer formation is strongly influenced by the surface roughness observed in FESEM (Figs. 6 & 7). Additionally, the charge-discharge behaviour of the SCs at different twisting angles is shown in Fig. S5.

In order to assess the electrochemical performance, the energy density (E_d) and power density (P_d) of fabricated SCs were also calculated using Eqs. (3) & (4). Under no load conditions, the SC exhibits an E_d of 2.534 Wh kg^{-1}, and 160 W kg^{-1} is the P_d. While applying twisting conditions (60°, 120°, and 180°), the SC exhibited E_d decreases to 1.2, 0.877 and 0.46 Wh kg^{-1} at 20 mA g^{-1}. Similarly, at 18 mAg^{-1}, the SC exhibits an E_d of 2.89 Wh Kg^{-1} and P_d of 143.99 W kg^{-1} for no-load conditions. When bending is applied, E_d decreased by 11.5% at 60°and by 25% at 90°. While folding and washing decrease by 17.8% and 15.15%, respectively, with respect to the no-load condition. However, the P_d remains relatively constant across all conditions. This phenomenon demonstrates that the SC can deliver instantaneous power under any condition, highlighting its suitability for flexible energy storage in wearable electronics.

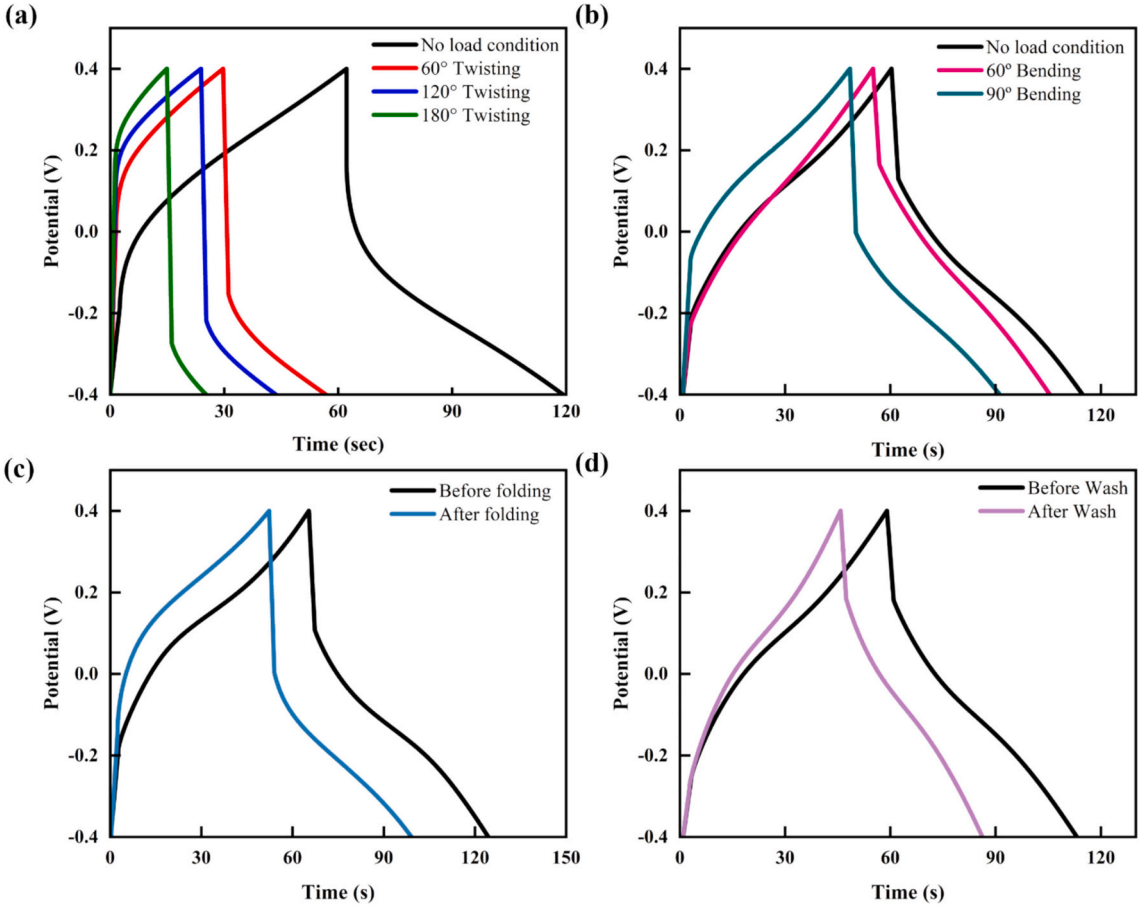

Fig. 13. The GCD behaviour of the flexible SCs: (a) Twisting condition, (b) bending condition, (c) folding condition and (d) after washing condition.

3.2.3. Electrochemical impedance spectroscopic (EIS) analysis of SCs

To gain a deeper understanding of ion-transport behaviour and electrical resistances, an EIS analysis of SCs with and without twisting was carried out. As twisted SC shows lower performance, further EIS analysis was focused on this. The Nyquist plots, Bode plot and equivalent circuit for SCs with and without twisting are presented in Fig. 14. The impedance spectra demonstrated a near-vertical line at low frequencies, approaching 45° as observed Fig. 14(a). Such behaviour is indicative of capacitive behaviour and suggests rapid diffusion of ions within the electrode [54]. A closer examination of the Nyquist plot (Fig. 14(b)) at twisting at 60° reveals a semicircle at high frequency. The Bode plot is presented in Fig. 14(c). Based on the nature of the curve, an equivalent circuit was designed as depicted in Fig. 14(d).

The charge transfer is faced with a small restriction at the interface. The circuit consists of a R_{ESR} followed by two parallel R_{ct} & constant phase element (*CPE*). The diameter of this semicircle represents the charge transfer resistance (R_{ct}). R_{ct} represents the interfacial/contact resistance linked to electron transfer across the electrode surface and near-surface ionic access. Furthermore, the equivalent series resistance (R_{ESR}) can be determined where the high-frequency portion of the plot intersects the real axis. This R_{ESR} value accounts for the resistance of the electrolyte and the contact resistance at the interface between the electrode and the electrolyte. As illustrated in Fig. 14(d), the SCs without twisting demonstrate lower R_{ct} (270 Ω) and R_{ESR} (1.09 kΩ) than the twisted SCs. This is due to the interruption of the free movement of ions during twisting, which creates narrower passages for ions to flow, as shown in Fig. 11(b). The increase in R_{ESR} with increasing twist angle directly reflects strain-induced degradation of electrical connectivity and increased contact resistance under torsional deformation. The derived value of R_{ct} and R_{ESR} is provided in Table S1. The elevated R_{ESR} values in the twisted SCs suggest the development of higher intrinsic resistance within the deposited graphite material. Similarly, the higher R_{ct} values observed in the twisted samples indicate a significant obstacle to ion transport at the electrode-electrolyte interface [56]. The first branch corresponds to the high-to-mid frequency range, representing interfacial charge transport at the electrode-electrolyte interface while *CPE* represent the non-ideal double-layer capacitance arising from surface roughness [26]. The second branch demonstrates the mid-to-low frequency region, representing distributed charge storage and transport within the graphite electrode. *R* is associated with ion transport resistance within deeper pore networks, while *CPE* corresponds to non-ideal capacitive behaviour related to slower ion adsorption/desorption processes in less accessible regions of the electrode [57]. EIS was employed to investigate the effect of torsional deformation on the charge transport and interfacial behaviour of the SC. The Nyquist and Bode plots recorded at twisting angles of 0°, 60°, 120°, and 180° were fitted using the equivalent circuit shown in Fig. S5. The Bode plots further support this interpretation. As the twisting angle increases, the magnitude of impedance rises across the entire frequency range. On the other hand, the phase angle's maximum value decreases and shifts toward (14°, 10°, 8° and 7°) lower frequencies. This shift corresponds to an increase in the characteristic relaxation time constant, indicating charge movement [48]. These changes confirm that during twisting combination of torsional and shear strain introduces significant limitations in both electronic and ionic transport processes. Bode plots at different twisting angles are shown in Fig. S5.

Overall, the EIS results demonstrate that the performance degradation of twisted devices originates from increased series resistance and distributed transport resistance, rather than solely from narrowed ion pathways. The equivalent circuit analysis thus provides a clear physical picture linking torsional deformation to loss of conductivity, increased interfacial resistance, and reduced capacitive efficiency, which explains the electrochemical trends observed in CV and GCD measurements.

3.2.4. Cycle stability analysis

The long-term cycling stability of the SC after 5000 cycles under various mechanical conditions, including the undeformed state, twisting at 180°, bending at 90°, folding, and washing, was analysis. Fig. 15

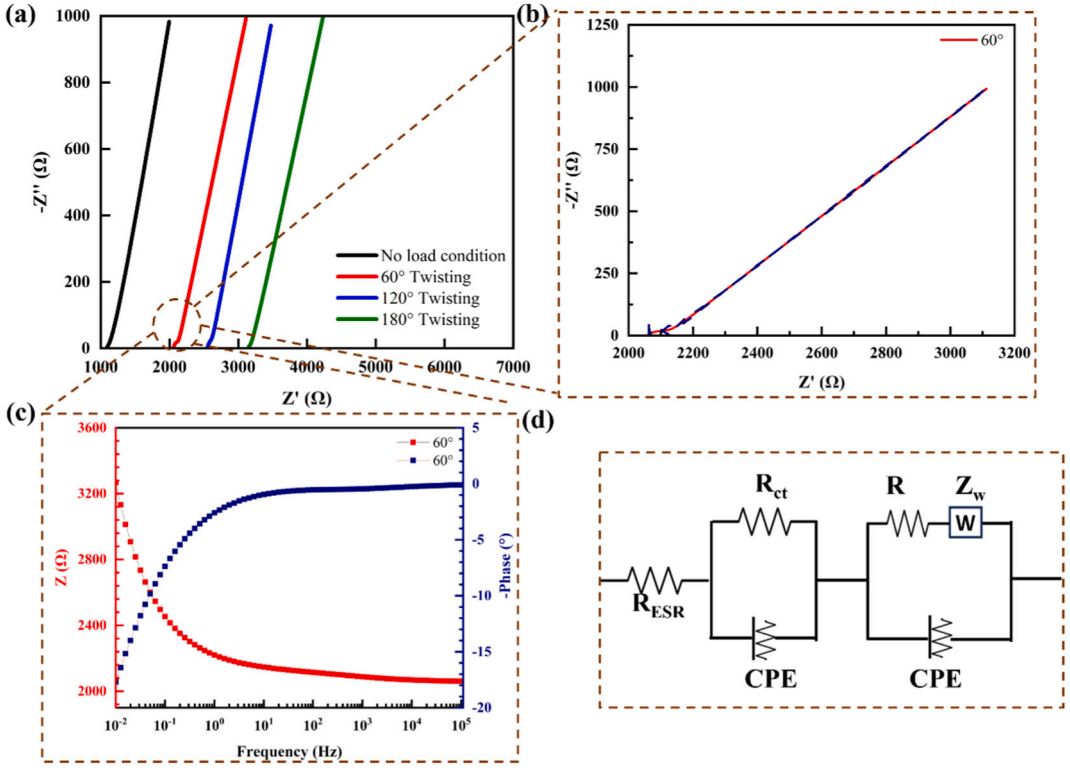

Fig. 14. Electrochemical performance of the flexible energy storage device: Electrochemical impedance spectroscopy at (a) different twisting angles, (b) equivalent circuit corresponding to the Nyquist plot.

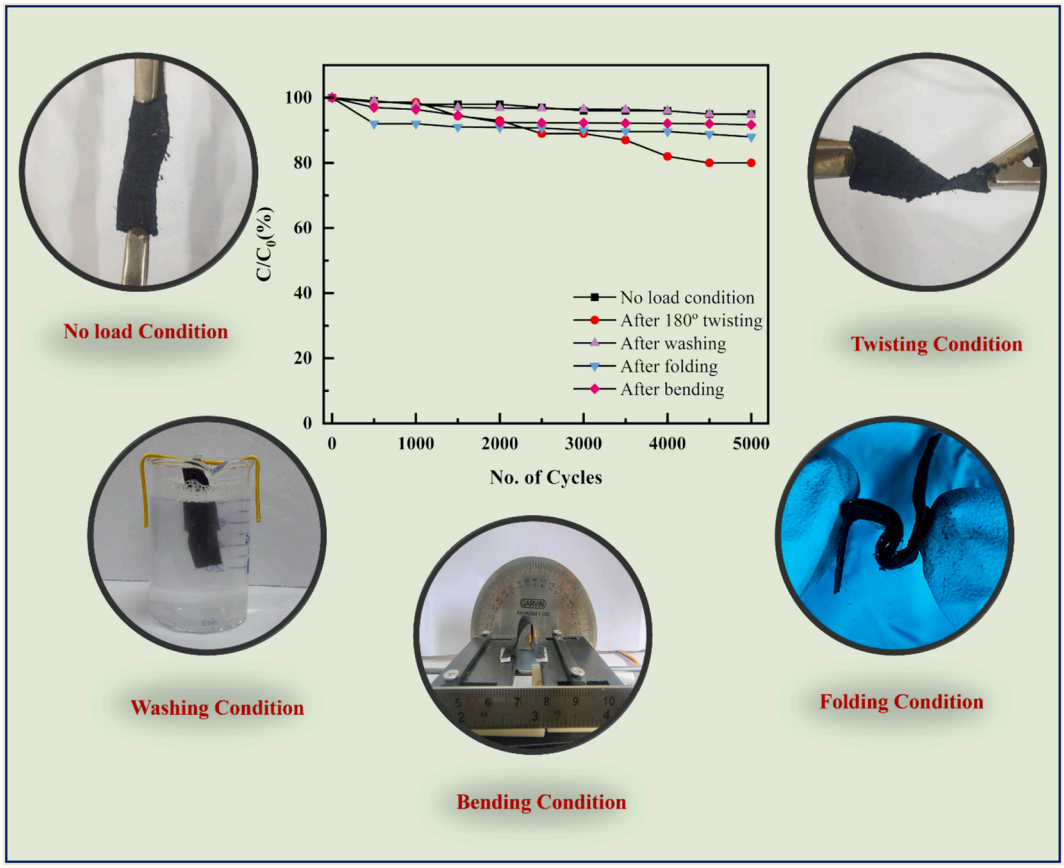

Fig. 15. Illustrate the cycle stability of SC after different mechanical deformation and washing condition.

represents the capacity retention of SC after 5000 cycles at different conditions. At no load condition SC can retain up to 95%, whereas twisted SC retain up to 84%. This behaviour is attributed to the accumulation of torsional and shear strain, which progressively disrupts conductive pathways within the graphite electrode [58]. In comparison, bending at 90° results in higher capacitance retention values of 91.7%, indicating that the SC can better tolerate uniaxial deformation [29]. Folding causes a moderate decline in capacitance (88%) due to the induced strain in multiple localised regions of the device. After exposure to detergent washing (5 cycles of 1 min each), the SC retains 94% of its initial capacitance, demonstrating acceptable electrochemical durability [59]. Overall, these results confirm that torsional deformation imposes the most severe limitation on cycling stability, whereas bending, folding, and washing exert comparatively smaller effects on long-term electrochemical performance.

Table 1 presents a quantitative comparison of the existing research work with our work for enhanced analysis.

From Table 1, it is clearly observed that using base materials, a very low C_s can be achieved, whereas using our approach, storage capacity and cycle stability can be improved.

4. Conclusion

This study introduces a novel approach to fabricating flexible supercapacitors (SCs) using 3D printing-assisted, uniformly coated textiles, which offers significant advantages in electrode deposition and

Table 1
comparative table benchmarking their device's key metrics (C_s, E_d, P_d, flexibility retention) against other published textile-based SCs.

Electrode	Specific capacitance (C_s) [Fg^{-1}]	Energy density (E_d) [Wh kg^{-1}]	Power density (P_d) [Wkg^{-1}]	Durability	Remarks	Ref
PEDOT: PSS	8.94	1.36	329.70	75% after 4000 cycles	3.18 times lower C_s and 21% lower cycle stability	[60]
Graphene	11.2	22.1	48.5	Completely discharge time 28.05 min	2.54 times lower C_s	[61]
CNT	8.01	6.30	2.72	96% retention after 5000 cycles	3.55 times lower C_s and 1% higher cycle stability	[62]
Carbon fibre	0.62	–	–	Retention after 1000 cycles	46 times lower C_s	[59]
Carbon threads	2.3	0.386	46.4	Stable over 100 cycles	12.4 times lower C_s	[63]
PVDF	20.13	–	–	92.5% retention after 150 cycles	1.41 times lower C_s and 2.63% lower cycle stability	[64]
Graphene	4.82	0.67	252.2	95% retention after 1000 cycles	6 times lower C_s and cycle stability same	[65]
Graphite	20.35	2.534	160	95% retention after 5000 cycles		This work

device performance. The key benefits of this method and conclusions are:

i) The attachment of **textiles to a 3D-printed frame** creates a wrinkle-free surface, enabling uniform electrode material deposition. This design overcomes the inherent unevenness of flexible textile substrates, ensuring consistent electrochemical properties across the entire electrode surface and minimizing defects that could compromise performance.
ii) The volumetric deposition technique, combined with a **hydrothermal process**, significantly **increases the mass loading** of active materials per unit area. This enhancement directly contributes to improved energy and power densities of the SCs.
iii) Integrating the hydrothermal process further enhances the **Coulombic efficiency by up to 91% under 180° twisting angle** and uniformity of material deposition, promoting stronger adhesion and a more even distribution of electrode materials on the textile substrate.
iv) This SC can deliver **160 W kg^{-1} power density** under any twisting angle without reducing its efficiency. This process not only enhances the electrochemical behaviour by improving ion accessibility and charge transfer efficiency. This also strengthens the mechanical stability of the electrode, allowing it to maintain performance under repeated deformation.
v) The fabricated flexible SC can retain cycle stability of **95%**, **84%**, **91.7%**, **88%**, and **94%**, respectively, at no-load, twisting, bending, folding, and washing conditions. This stability is observed due to the approach to the fabrication process.

In conclusion, this innovative approach addresses critical challenges in developing high-performance flexible SCs. These improvements have significant implications for advancing wearable electronics and smart textiles, offering promising future research and development opportunities in the flexible ESDs.

CRediT authorship contribution statement

Soumili Sahoo: Writing – original draft, Visualization, Validation, Methodology, Investigation, Formal analysis, Data curation, Conceptualization. **Viney Ghai:** Writing – review & editing, Visualization, Investigation, Data curation. **Roland Kádár:** Writing – review & editing, Supervision, Resources, Funding acquisition. **Tribeni Roy:** Writing – review & editing, Resources, Project administration, Funding acquisition, Conceptualization.

Declaration of competing interest

The authors declare that they have no known competing financial interests or personal relationships that could have appeared to influence the work reported in this paper.

Acknowledgements

SS & TR are grateful to Science and Engineering Research Board (SERB), Government of India, for generous funding through the Startup Research Grant (SRG/2021/000741). All the authors are thankful to the Swedish Foundation for International Cooperation in Research and Higher Education (STINT) for providing funds for carrying out the research work.

Appendix A. Supplementary data

Supplementary data to this article can be found online at https://doi.org/10.1016/j.est.2026.121017.

Data availability

Data will be made available on request.

References

[1] S.M.A. Iqbal, I. Mahgoub, E. Du, M.A. Leavitt, W. Asghar, Advances in healthcare wearable devices, NPJ Flexible Electron. 5 (1) (2021) 1–14, https://doi.org/10.1038/s41528-021-00107-x.
[2] X. Qu, et al., Foldable and wearable supercapacitors for powering healthcare monitoring applications with improved performance based on hierarchically co-assembled CoO/NiCo networks, J. Colloid Interface Sci. 634 (2023) 715–729, https://doi.org/10.1016/j.jcis.2022.12.005.
[3] U. Heredia-Rivera, et al., Cold atmospheric plasma deposition of antibacterial polypyrrole-silver nanocomposites on wearable electronics for prolonged performance, J. Mater. Chem. C 12 (31) (2024) 11861–11876, https://doi.org/10.1039/d4tc00844h.
[4] S. Raut, G. Jaisinghani, N. Doshi, G. Gaikwad, Smart warfare: designing intelligent vests for enhanced military operations, in: 7th Int. Conf. Inven. Comput. Technol. ICICT 2024, No. Icict, 2024, pp. 1016–1022, https://doi.org/10.1109/ICICT60155.2024.10544719.
[5] K.C. Tsay, L. Zhang, J. Zhang, Effects of electrode layer composition/thickness and electrolyte concentration on both specific capacitance and energy density of supercapacitor, Electrochim. Acta 60 (2012) 428–436, https://doi.org/10.1016/j.electacta.2011.11.087.
[6] L. Yin, J. Wang, Wearable energy systems: what are the limits and limitations? Natl. Sci. Rev. 10 (1) (2023) 2022–2024, https://doi.org/10.1093/nsr/nwac060.
[7] M. Shao, et al., PEDOT/ZnO@nickel foam as flexible electrode material for high-performance supercapacitor, J. Mater. Sci. Mater. Electron. 35 (2) (2024) 1–10, https://doi.org/10.1007/s10854-024-11951-8.
[8] D.S. Gaikwad, et al., SILAR-synthesized Co3O4/Bi2O3 on copper substrate nanocomposite electrode and asymmetric Co3O4/Bi2O3/CuO: AC solid-state device in supercapacitor, J. Mater. Sci. Mater. Electron. 35 (7) (2024) 1–18, https://doi.org/10.1007/s10854-024-12220-4.
[9] S. Yeasmin, S. Talukdar, D. Mahanta, Paper based pencil drawn multilayer graphene-polyaniline nanofiber electrodes for all-solid-state symmetric supercapacitors with enhanced cyclic stabilities, Electrochim. Acta 389 (2021) 138660, https://doi.org/10.1016/j.electacta.2021.138660.
[10] T. Kshetri, D.D. Khumujam, T.I. Singh, Y.S. Lee, N.H. Kim, J.H. Lee, Co-MOF@MXene-carbon nanofiber-based freestanding electrodes for a flexible and wearable quasi-solid-state supercapacitor, Chem. Eng. J. 437 (P1) (2022) 135338, https://doi.org/10.1016/j.cej.2022.135338.
[11] X. Xu, Y. Liu, P. Dong, P.M. Ajayan, J. Shen, M. Ye, Mesostructured CuCo2S4/CuCo2O4 nanoflowers as advanced electrodes for asymmetric supercapacitors, J. Power Sources 400 (July) (2018) 96–103, https://doi.org/10.1016/j.jpowsour.2018.08.012.
[12] Y. Wang, X. Wu, Y. Han, T. Li, Flexible Supercapacitor: Overview and Outlooks, Elsevier Ltd., Oct. 01, 2021, https://doi.org/10.1016/j.est.2021.103053.
[13] S. Rani, et al., Flexible self-powered supercapacitors integrated with triboelectric nanogenerators, Energy Storage Mater. (2024) 103977, https://doi.org/10.1016/j.ensm.2024.103977.
[14] A. Grube, et al., Wearable textile supercapacitors: material advancements and applications, J. Energy Storage 99 (PB) (2024) 113228, https://doi.org/10.1016/j.est.2024.113228.
[15] A. Hayat, et al., Enhanced asymmetric supercapacitor and oxygen evolution reaction performance by sugarcane molasses-generated Co3O4 nanostructures, Int. J. Hydrog. Energy 92 (September) (2024) 895–906, https://doi.org/10.1016/j.ijhydene.2024.10.253.
[16] R. Sahu, T.K. Shivasharma, M.C. Rath, S.J. Keny, B.R. Sankapal, Photochemically synthesized tin oxide nanoparticles: electrode to device grade solid-state supercapacitor, J. Energy Storage 101 (PB) (2024) 113957, https://doi.org/10.1016/j.est.2024.113957.
[17] Y.C. Goswami, S. Begzaad, Printable supercapacitors and their printing technologies: a review, Energy Storage 6 (4) (2024) 1–31, https://doi.org/10.1002/est2.666.
[18] Vidhi, M. Sadiq, A.K. Singh, O.P. Thakur, Fabrication and electrochemical insights into advanced rGO-modified ternary Cu-doped NiFe2O4/TiO_2 electrodes for high performance supercapacitors, Ceram. Int. (2024), https://doi.org/10.1016/j.ceramint.2024.12.016 (no. December).
[19] T. Neff, A. Krueger, A spray coated high performing metal-free onion-like carbon supercapacitor for sustainable energy storage, Electrochem. Commun. 167 (July) (2024) 107798, https://doi.org/10.1016/j.elecom.2024.107798.
[20] Y. Lin, X. Xiang, D. Mou, X. Pu, P. Li, X. Zhu, Reduced graphene oxide-assisted hydrothermal post-treatment of β-nickel hydroxide nanosheets/nickel foam hybrid electrode for high performance supercapacitors, J. Energy Storage 92 (May) (2024) 112198, https://doi.org/10.1016/j.est.2024.112198.
[21] T. Guan, L. Shen, N. Bao, Hydrophilicity improvement of graphene fibers for high-performance flexible supercapacitor, Ind. Eng. Chem. Res. 58 (37) (2019) 17338–17345, https://doi.org/10.1021/acs.iecr.9b02504.
[22] B. Wang, W. Song, P. Gu, L. Fan, Y. Yin, C. Wang, A stretchable and hydrophobic polypyrrole/knitted cotton fabric electrode for all-solid-state supercapacitor with excellent strain capacitance, Electrochim. Acta 297 (2019) 794–804, https://doi.org/10.1016/j.electacta.2018.12.042.

[23] B. Eghan, E.A. Ofori, R. Kanyire, B. Tawiah, R. Acquaye, Systematic review of conductive inks for e-textiles: formulation, printing methods, challenges, and opportunities 12 (1) (2025) 1–17, https://doi.org/10.1177/24723444241303970.

[24] L. Hu, et al., Stretchable, porous, and conductive energy textiles, Nano Lett. 10 (2) (2010) 708–714, https://doi.org/10.1021/nl903949m.

[25] M. Pasta, F. la Mantia, L. Hu, H.D. Deshazer, Y. Cui, Aqueous supercapacitors on conductive cotton, Nano Res. 3 (6) (2010) 452–458, https://doi.org/10.1007/s12274-010-0006-8.

[26] G. Yu, et al., Solution-processed graphene/MnO2 nanostructured textiles for high-performance electrochemical capacitors, Nano Lett. 11 (7) (2011) 2905–2911, https://doi.org/10.1021/nl2013828.

[27] Y. Fu, et al., Fiber supercapacitors utilizing pen ink for flexible/wearable energy storage, Adv. Mater. 24 (42) (2012) 5713–5718, https://doi.org/10.1002/adma.201202930.

[28] J. Wen, et al., Flexible coaxial-type fiber solid-state asymmetrical supercapacitor based on Ni3S2 nanorod array and pen ink electrodes, J. Power Sources 324 (2016) 325–333, https://doi.org/10.1016/j.jpowsour.2016.05.087.

[29] M. Zhou, H. Zhang, Y. Qiao, C.M. Li, Z. Lu, A flexible sandwich-structured supercapacitor with poly(vinyl alcohol)/H3PO4-soaked cotton fabric as solid electrolyte, separator and supporting layer, Cellulose 25 (6) (2018) 3459–3469, https://doi.org/10.1007/s10570-018-1786-3.

[30] X. Ye, Y. Zhu, H. Jiang, Z. Yue, C. Jia, Improving performance of fibriform supercapacitor based on cotton thread by uncoiling dip-coating procedure, IOP Conf. Ser. Mater. Sci. Eng. 677 (5) (2019), https://doi.org/10.1088/1757-899X/677/5/052009.

[31] M. Barakzehi, M. Montazer, F. Sharif, T. Norby, A. Chatzitakis, MOF-modified polyester fabric coated with reduced graphene oxide/polypyrrole as electrode for flexible supercapacitors, Electrochim. Acta 336 (2020) 135743, https://doi.org/10.1016/j.electacta.2020.135743.

[32] B. Moradi, D. Wang, G.G. Botte, Carbon-coated Fe3O4 nanospindles as solid electrolyte interface for improving graphite anodes in lithium ion batteries, J. Appl. Electrochem. 50 (3) (2020) 321–331, https://doi.org/10.1007/s10800-019-01393-0.

[33] B. wen Deng, Y. Yang, Y. xin Liu, B. Yin, M. bo Yang, Dipping fabrication of rHGO@NiO@NF flexible supercapacitor electrode and its potential in bendable electronic devices, Electrochim. Acta 399 (2021) 139359, https://doi.org/10.1016/j.electacta.2021.139359.

[34] H. Lee, G. Jung, K. Keum, J.W. Kim, H. Jeong, Y.H. Lee, D.S. Kim, J.S. Ha, A textile-based temperature-tolerant stretchable supercapacitor for wearable electronics, Adv. Funct. Mater. 31 (50) (2021) 2106491, https://doi.org/10.1002/adfm.202106491.

[35] Y. Zhang, Materials Chemistry Frontiers Oxygen Vacancies for Enhanced Water Oxidation †, 2020, pp. 1993–1999, https://doi.org/10.1039/d0qm00300j.

[36] L. Flores-Larrea, et al., Highly efficient textile supercapacitors fabricated with graphene/NiO:Yb electrodes printed on cotton fabric, J. Alloys Compd. 886 (2021), https://doi.org/10.1016/j.jallcom.2021.161219.

[37] G. D'Altri, et al., Preparation and characterization of self-healing PVA-H2SO4 hydrogel for flexible energy storage, ACS Omega 9 (6) (2024) 6391–6402, https://doi.org/10.1021/acsomega.3c05392.

[38] Y. Guo, Y. Wei, H. Li, T. Zhai, Layer structured materials for advanced energy storage and conversion, Small 13 (45) (2017) 1–22, https://doi.org/10.1002/smll.201701649.

[39] W. Luo, X. Li, J.Y. Chen, All-fabric flexible supercapacitor for energy storage 49 (8) (2020) 1061–1077, https://doi.org/10.1177/1528083718804208.

[40] C. Wang, et al., Ni (II) doping induced lattice distortion in Zn 3 In 2 S 6/BiOBr-OVs for boosting photocatalytic removal of antibiotics and Cr (VI) performance 324 (June) (2023).

[41] A.A. Khomich, V. Kononenko, O. Kudryavtsev, E. Zavedeev, A.V. Khomich, Raman study of the diamond to graphite transition induced by the single femtosecond laser pulse on the (111) face, Nanomaterials 13 (1) (2023), https://doi.org/10.3390/nano13010162.

[42] K. Gong, et al., A flexible supercapacitor with high energy density and wide range of temperature tolerance using a high-concentration aqueous gel electrolyte, Electrochim. Acta 475 (September 2023) (2024) 143585, https://doi.org/10.1016/j.electacta.2023.143585.

[43] C.S. Pathak, Samir Kumar (Eds.), Recent developments in atomic force microscopy and Raman spectroscopy for materials characterization, 2022.

[44] M. Saquib, et al., Printed flexible supercapacitor from conductive ink of graphite nanocomposite blended with Co3O4 to facilitate the fabrication of energy storage device, J. Energy Storage 72, no. PE (2023) 108800, https://doi.org/10.1016/j.est.2023.108800.

[45] H. Badenhorst, Microstructure of natural graphite flakes revealed by oxidation: limitations of XRD and Raman techniques for crystallinity estimates, Carbon N. Y. 66 (2014) 674–690, https://doi.org/10.1016/j.carbon.2013.09.065.

[46] L.F. Aval, M. Ghoranneviss, G.B. Pour, Graphite nanoparticles paper supercapacitor based on gel electrolyte, Mater. Renew. Sustain. Energy 7 (4) (2018) 1–11, https://doi.org/10.1007/s40243-018-0136-6.

[47] Wenchao Li, Tingting Hao, Jian Hao, Tenghao Ma, An Li, Songlin Yang, Jing Wang, Construction of high-performance hybrid supercapacitor devices by V-doped flower-like $Fe_2(MoO_4)_3$ and SnO_2/CNTs, Chem. Eur. J. 31 (23) (2025) e202500410, https://doi.org/10.1002/chem.202500410.

[48] H. Li, Y. Yu, L. Liu, L. Liu, Y. Wu, One-step electrochemically expanded graphite foil for flexible all-solid supercapacitor with high rate performance, Electrochim. Acta 228 (2017) 553–561, https://doi.org/10.1016/j.electacta.2017.01.063.

[49] X. Ye, Q. Zhou, C. Jia, Z. Tang, Z. Wan, X. Wu, A knittable fibriform supercapacitor based on natural cotton thread coated with graphene and carbon nanoparticles, Electrochim. Acta 206 (2016) 155–164, https://doi.org/10.1016/j.electacta.2016.04.100.

[50] N. Yu, et al., Facile fabrication of low-cost and scalable graphite tape as novel current collectors for flexible supercapacitors, J. Alloys Compd. 861 (2021) 158476, https://doi.org/10.1016/j.jallcom.2020.158476.

[51] Shasha Jiao, Tiehu Li, Chuanyin Xiong, Chen Tang, Alei Dang, Hao Li, Tingkai Zhao, A facile method of preparing the asymmetric supercapacitor with two electrodes assembled on a sheet of filter paper, Nanomaterials 9 (9) (2019) 1338, doi:0.3390/nano9091338.

[52] N.A. Aimanova, et al., Development of the all-solid-state flexible supercapacitor membranes via RAFT-mediated grafting and electrospun nanofiber modification of track-etched membranes, RSC Adv. 15 (8) (2025) 6260–6280, https://doi.org/10.1039/d4ra08055f.

[53] J.E. Yoo, J. Bae, Novel flexible supercapacitors fabricated by simple integration of electrodes, binders, and electrolytes into glass fibre separators, J. Korean Electrochem. Soc. 17 (4) (2014) 237–244, https://doi.org/10.5229/jkes.2014.17.4.237.

[54] G. Xin, et al., Electrochimica acta preparation of self-supporting graphene on fl exible graphite sheet and electrodeposition of polyaniline for supercapacitor, Electrochim. Acta 167 (2015) 254–261, https://doi.org/10.1016/j.electacta.2015.03.181.

[55] E. Frackowiak, Carbon materials for supercapacitor application, Phys. Chem. Chem. Phys. 9 (15) (2007) 1774–1785, https://doi.org/10.1039/B618139M.

[56] S. Kulandaivalu, N. Suhaimi, Y. Sulaiman, Unveiling high specific energy supercapacitor from layer-by-layer assembled polypyrrole/graphene oxide| polypyrrole/manganese oxide electrode material, Sci. Rep. 9 (1) (2019) 1–10, https://doi.org/10.1038/s41598-019-41203-3.

[57] T. Purkait, G. Singh, D. Kumar, M. Singh, R.S. Dey, High-performance flexible supercapacitors based on electrochemically tailored three-dimensional reduced graphene oxide networks, Sci. Rep. (2018) 1–14, https://doi.org/10.1038/s41598-017-18593-3 (no. May 2017).

[58] C. Meng, C. Liu, L. Chen, C. Hu, S. Fan, Polymer Supercapacitors, 2010, pp. 4025–4031, https://doi.org/10.1021/nl1019672.

[59] T. Henriques, C. Cidade, A. Marques, I.M.M. Ferreira, A.C. Baptista, Carbon Threads Supercapacitors for Washable E-Textile Applications: Configurations and Electrochemical Performance, 2024, https://doi.org/10.1021/acsaenm.3c00723.

[60] L. Manjakkal, A. Pullanchiyodan, N. Yogeswaran, E.S. Hosseini, A Wearable Supercapacitor Based on Conductive PEDOT: PSS-Coated Cloth and a Sweat Electrolyte vol. 1907254, 2020, https://doi.org/10.1002/adma.201907254.

[61] Y.K. Kshetri, C.R. Garcia, S.W. Lee, J. Oliva, Highly efficient textile supercapacitors fabricated with graphene/NiO_Yb electrodes printed on cotton fabric, J. Alloys Compd. 886 (2021) 161219, https://doi.org/10.1016/j.jallcom.2021.161219.

[62] R.S. Costa, A. Guedes, C. Pereira, Materials Fabrication of All-Solid-State Textile Supercapacitors Based on Industrial-Grade Multi-Walled Carbon Nanotubes for Enhanced Energy Storage, 2020, pp. 10121–10141, https://doi.org/10.1007/s10853-020-04709-0.

[63] N. Lima, A.C. Baptista, B.M.M. Faustino, S. Taborda, A. Marques, I. Ferreira, Carbon threads sweat-based supercapacitors for electronic textiles, Sci. Rep. 10 (1) (2020) 1–9, https://doi.org/10.1038/s41598-020-64649-2.

[64] J. Sun, L.H. He, Q.L. Zhao, L.F. Cai, R. Song, Y.M. Hao, Research Article a Simple and Controllable Nanostructure Comprising Non-Conductive Poly (Vinylidene Fluoride) and Graphene Nanosheets for Supercapacitor vol. 6, no. 2, 2012, pp. 149–159, https://doi.org/10.1007/s11706-012-0163-7.

[65] S. Wang, B. Pei, X. Zhao, R.A.W. Dryfe, Highly porous graphene on carbon cloth as advanced electrodes for flexible all-solid-state supercapacitors, Nano Energy 2 (4) (2013) 530–536, https://doi.org/10.1016/j.nanoen.2012.12.005.